Fabrication of high speed and reliable 850nm oxide-confined VCSELs for 10Gb/s data communication

H. C. Kuo*[a], Y. H. Chang[a], Y. A. Chang[a], K. F. Tseng[a], L. H. Laih[a], S. C. Wang[a], H.C. Yu[b], C. P. Sung[b], H.P. Yang[b]

[a] Department of Photonics and Institute of Electro-optical Engineering, National Chiao-Tung University, Hsinchu, Taiwan, R. O. C,
[b] Opto-Electronics and System Laboratory, Industrial Technology Research Institute Hsin-Tsu 310, Taiwan, R.O.C.

Keywords: Strain-compensated, High-speed electronics, VCSELs, InGaAsP/InGaP, proton-implant

ABSTRATE

In this paper, we demonstrate high performance 850 nm InGaAsP/InGaP strain-compensated MQWs vertical-cavity surface-emitting lasers (VCSELs). These VCSELs exhibit superior performance with threshold currents of ~0.4 mA, and slope efficiencies of ~ 0.6 mW/mA. High modulation bandwidth of 14.5 GHz and modulation current efficiency factor of 11.6 GHz/(mA)$^{1/2}$ are demonstrated. We have accumulated life test data up to 1000 hours at 70°C/8mA. In addition, we also report a high speed planarized 850nm oxide-implanted VCSELs process that does not require semiinsulating substrates, polyimide planarization process, or very small pad areas, therefore very promising in mass manufacture.

1. INTRODUCTION

850 nm oxide-confined Vertical Cavity Surface Emitting Lasers (VCSELs) have become a standard technology for application in local area networks (LANs) from 1.25 Gb/s to 10Gb/s [1-4]. The low threshold current, high modulation bandwidth, and high modulation current efficiency make VCSELs an ideal source for high speed optical communication [5-7]._The low divergent angle and circular beam lead to efficiency fiber coupling and simpler packaging. The surface emission from the VCSELs also makes easy the 2-dimensional array integration and allows wafer level testing, in turns leading to low fabrication cost. The use of an Al-free InGaAsP based active region is an attractive alternative to the conventional (Al)GaAs active region for IR VCSELs. While edge emitting diode lasers with Al-free active regions have demonstrated performance and reliability surpassing AlGaAs-active devices [8-9]. In addition, theoretical calculations have predicted a lower transparency current density, high differential gain and better temperature performance in InGaAsP-strain active VCSELs in respect to lattice-matched GaAs quantum-well active devices [10]. These parameters are all very important in high speed and high temperature VCSEL design because the relaxation resonance frequency of the laser depends on the square root of the differential gain as well as the difference of operation current and threshold current [4]. The use of tensile-strained barriers like $In_{0.4}Ga_{0.6}P$ can provide strain compensation and reduce active region carrier leakage. Al-free materials are significantly less reactive to oxide level, compared to AlGaAs materials make them ideal for the reliable manufacture process [8]. Proton implanted VCSELs using strain $In_{0.18}Ga_{0.82}As_{0.8}P_{0.2}$ active-region has been demonstrated good performance [11]. In the first part of this paper, we demonstrated $In_{0.18}Ga_{0.82}As_{0.8}P_{0.2}/In_{0.4}Ga_{0.6}P$ strain-compensated MQWs (SC-MQWs) VCSELs with superior high speed performance [12]. DC, small signal, and large signal measurements were performed on SC-MQWs VCSELs with the initial reliability results. Cost and reliability are the important issues in commercial application. In the second part of this paper, we present a high speed planarized 850nm oxide-implanted VCSELs process that does not require semiinsulating substrates, polyimide planarization process, or very small pad areas, therefore very promising in mass manufacture.

Semiconductor and Organic Optoelectronic Materials and Devices,
edited by Chung-En Zah, Yi Luo, Shinji Tsuji, Proceedings of SPIE Vol. 5624
(SPIE, Bellingham, WA, 2005) · 0277-786X/05/$15 · doi: 10.1117/12.577050

Downloaded From: http://proceedings.spiedigitallibrary.org/ on 04/26/2014 Terms of Use: http://spiedl.org/terms

2. INGAASP/INGAP SC-MQW VCSEL

Fig. 1 shows the schematic structure of the SC-MQW VCSEL, which has been grown by low pressure metal organic chemical vapor deposition (MOCVD) on a semi-insulating (100) GaAs substrate. The group-V precursors are the hydride sources AsH_3 and PH_3. The trimethyl alkyls of gallium (Ga), aluminum (Al) and indium (In) are the group-III precursors. The dopant sources are Si_2H_6 and CBr_4 for the *n* and *p* dopants. The bottom n-type distributed Bragg reflector (DBR) consists of 35-period-$Al_{0.15}Ga_{0.85}As/Al_{0.9}Ga_{0.1}As$. The top p-type DBR consists of 23 pairs of $Al_{0.15}Ga_{0.85}As/Al_{0.9}Ga_{0.1}As$. The active layer consists of three $In_{0.18}Ga_{0.82}As_{0.8}P_{0.2}$/ $In_{0.4}Ga_{0.6}P$ (80Å/100Å) SC-MQWs surrounded by $Al_{0.6}Ga_{0.4}As$ cladding layer to 1λ-cavity. A 30nm thick $Al_{0.98}Ga_{0.02}As$ was introduced on the upper cavity spacer layer to form an oxide confinement. Finally, 1λ thickness of current spreading layer and heavily doped GaAs (p> $2x10^{19}$ cm^{-3}) contacting layer was grown. The n-type DBR was grown at 750°C. The quantum well region and p-type DBR were grown at 650°C. Growth interruptions of 5s, 10s, or 15s were introduced before and after $In_{0.18}Ga_{0.82}As_{0.8}P_{0.2}$ QW growth.

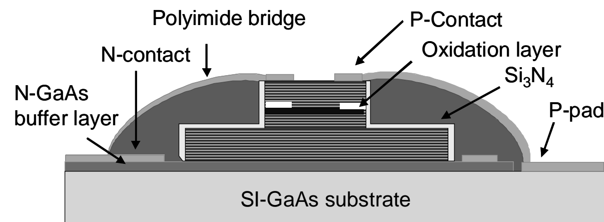

Fig. 1 Schematic cross section of high speed VCSEL structure.

Fig. 2 shows the comparison of photoluminescence spectra of $In_{0.18}Ga_{0.82}As_{0.8}P_{0.2}/In_{0.4}Ga_{0.6}P$ with different growth interruption times. The 5s growth interruption is not enough to evacuate residual As in the growth reactor, resulting in the carry-over of As into the $In_{0.4}Ga_{0.6}P$ barrier. The 15s growth interruption is so long that some impurities can be gettered at the interface or indium segregation after strained layer growth, resulting in the degradation of luminescence. The 10s growth interruption seems to give the best luminescence quality. The composition of SC-MQWs is characterized by high-resolution x-ray diffraction. The gain peak position = 835 nm was determined by photoluminescence while the FP-dip wavelength = 842 nm was determined by reflection measurement. The VCSELs were fabricated utilizing the processing described by Peters *et al.* to minimize capacitance while keeping reasonably low resistance [3]. The processing sequence included six photomasks to fabricate polyimide-planarized VCSELs with coplanar wave-guide probe pads. Device fabrication began with the formation of cylindrical mesas of 20 μm in diameter by etching the surrounding semiconductor to the bottom n-type mirror to a depth of 5 μm using a Reactive Ion Etching (RIE) system. The sample was wet-oxidized in a 420 °C steam environment for ~12 min to form the current aperture and provide lateral index guiding to the lasing mode. The oxidation rate was 0.6 μm/ min for the $Al_{0.98}Ga_{0.02}As$ layer, so the oxide extended 7.5 μm from the mesa sidewall. The VCSELs therefore have a 5 μm in diameter emitting aperture

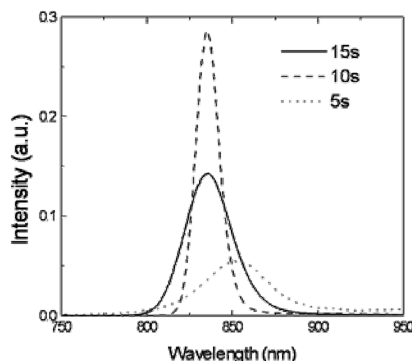

Fig. 2 PL spectra of SC-MQW with different growth interruption times

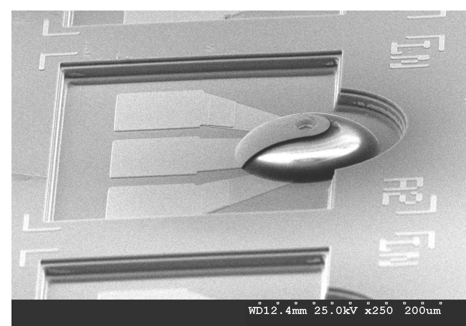

Fig. 3 SEM picture of the finished VCSEL

Downloaded From: http://proceedings.spiedigitallibrary.org/ on 04/26/2014 Terms of Use: http://spiedl.org/terms

defined by lateral oxidation. A 40 μm circular mesa were formed after oxidation using wet chemical etching (H_2O:H_2SO_4:H_2O_2 = 8:1:8) down to n-buffer layer. Following Si_3N_4 was deposited for passivation. Ti/Au was evaporated for the p-type contact ring, and AuGeNi/Au was evaporated onto the etched n–buffer layer to form the n-type contact which is connected to the semi-insulating substrate. Contacts were alloyed for 30 sec at 420 °C using RTA. After contact formation, photosensitive polyimide was spun on the sample for field insulation and planarization. Ti/Au with thicknesses of 200/3000Å were deposited for metal interconnects and coplanar waveguide probe-bond pads. Heat treatment after the metal deposition was utilized to improve metal-to-polyimide adhesion strength. Fig. 3 shows the SEM photo of a finished VCSEL.

Fig. 4 shows the typical light output and voltage versus current (LIV) curves of the SC-MQWs InGaAsP/InGaP VCSEL at room temperature and 85°C under CW operation. These VCSELs exhibit kink-free current-light output performance with threshold currents ~0.4 mA, and slope efficiencies ~ 0.6 mW/mA. The threshold current change with temperature is less than 0.2 mA and the slope efficiency drops by less than ~30% when the substrate temperature is raised from room temperature to 85°C. This is superior to the properties of GaAs/AlGaAs VCSELs with similar size [13]. The resistance of our VCSELs is ~95 Ohm and capacitance is ~0.1 pF. As a result, the devices are limited by the parasitics to a frequency response of approximately 15 GHz. The lateral mode characteristics is an important feature since it strongly affects the transmission properties. Fig. 5 shows the emission spectrum of a VCSEL at an operating current of 6 mA. This spectrum was recorded with an optical spectrum analyzer (Advantest 8381A) with spectral resolution of 0.1 nm. Two dominate modes were observed at 844.2 nm and 843.7 nm. The root-mean-squared (RMS) spectral linewidths at 2, 6, 8 mA are 0.15, 0.37, and 0.4 nm respectively, which can fulfill the requirement (<= 0.45 nm) of 10Gbps data transmission.[14]

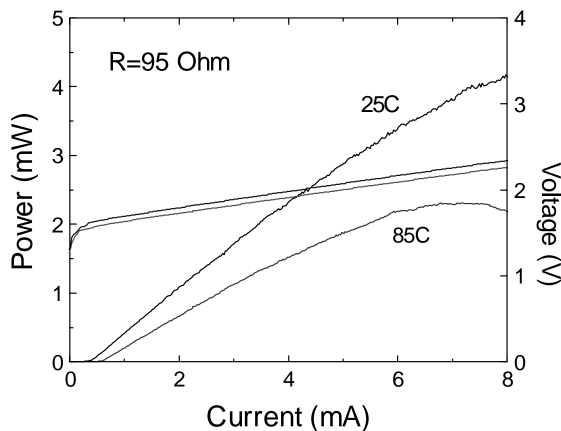

Fig. 4 SC-MQWs InGaAsP/InGaP VCSEL light output and voltage versus current (LIV) curves at room temperature and 85°C.

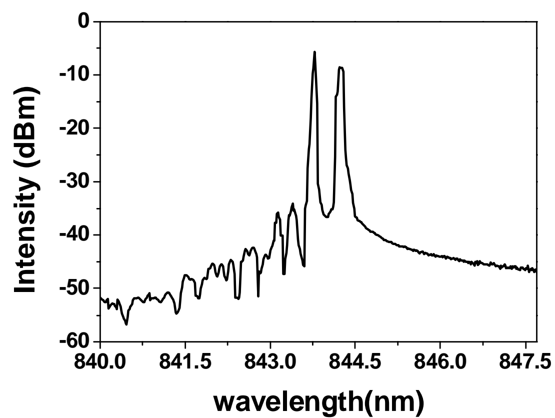

Fig. 5 Optical spectrum at 6 mA of the VCSEL

The small signal response of VCSELs as a function of bias current was measured using a calibrated vector network analyzer (Agilent 8720ES) with on-wafer probing and 50 μm multimode optical fiber connected to a New Focus 25GHz photodetector. Fig. 6 shows the measured (dashed lines) and fitted (solid lines) small-signal frequency response of a 5 μm VCSEL at different bias current levels. The modulation frequency is increased with increasing bias current until flattening at a bias of approximately 5mA. With only 3mA (5mA) of bias current, the maximum 3dB modulation frequency response is measured to be ~13 (14.5) GHz at 25 °C and is suitable for 12.5 Gb/s operation. The measured data were fit to a general 3-pole modulation transfer function [15, 16]

$$H(f) = C\left(\frac{fr^2}{fr^2 - f^2 + j\frac{f}{2\pi}\gamma}\right)\left(\frac{1}{1 + j\left(\frac{f}{fp}\right)}\right) \quad \text{...(1)}$$

where f is modulation frequency, f_p is parasitic roll off frequency, f_r is resonant frequency and γ is damping rate. Fig. 7 shows the 3dB modulation frequency as a function the square root of the difference in current above threshold. The relaxation resonance frequency is found saturate for driving currents above 3mA. By fitting the lowest current points in

Downloaded From: http://proceedings.spiedigitallibrary.org/ on 04/26/2014 Terms of Use: http://spiedl.org/terms

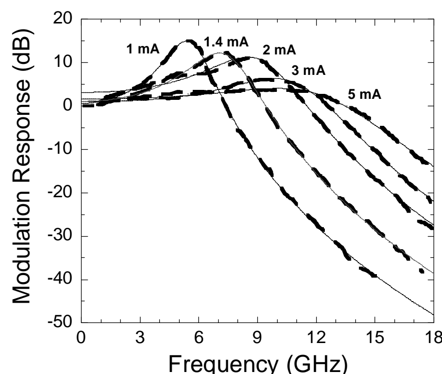

Fig. 6 SC-MQWs InGaAsP/InGaP VCSEL light output and voltage versus current (LIV) curves at room temperature and 85°C.

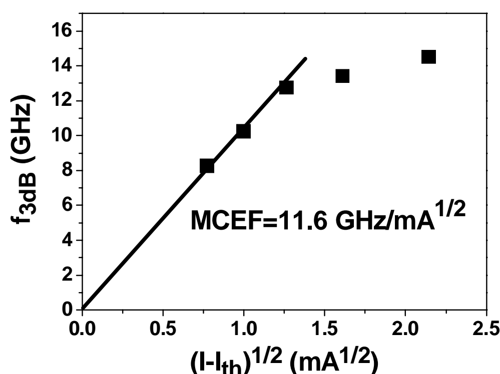

Fig. 7 3dB frequency as a function of square root of current above threshold current.

Fig. 7, we obtain a modulation current efficiency of 11.6 GHz/(mA)$^{1/2}$[17]. This is higher than GaAs/AlGaAs VCSELs with similar size [6, 18] and is comparable with oxide confined VCSELs with InGaAs based quantum wells [7, 15]. Plotting the damping rate γ versus f_r^2 reveals a K-factor of 0.3 ns. Neglecting heating effects and external parasitics, the intrinsic bandwidth was found to be 29.6GHz using the relation f_{max}=. $\sqrt{2}(2\pi/K)$

To measure the high-speed VCSEL under large signal modulation, microwave and lightwave probes were used in conjunction with a 12.5-Gb/s pattern generator and a 12-GHz photoreceiver. The eye diagrams were taken for back-to-back (BTB) transmission on SC-MQWs InGaAsP/InGaP VCSEL. As shown in Fig. 8(a), the room temperature eye diagram of our VCSEL biased at 4 mA with data up to 12.5 Gb/s and 6dB extinction ratio has a clear open eye pattern indicating good performance of the VCSELs. The rise time T_r is 28 ps and fall time T_f is 41 ps with jitter (p-p)=20 ps. The VCSELs also show superior performance at high temperature. Fig. 8 (b) demonstrated the high speed performance of our VCSELs (biased at 5mA) with reasonably open eye-diagrams at 12.5 Gb/s and 6dB extinction ratio at 85°C. This further confirms the superior performance of our VCSELs.

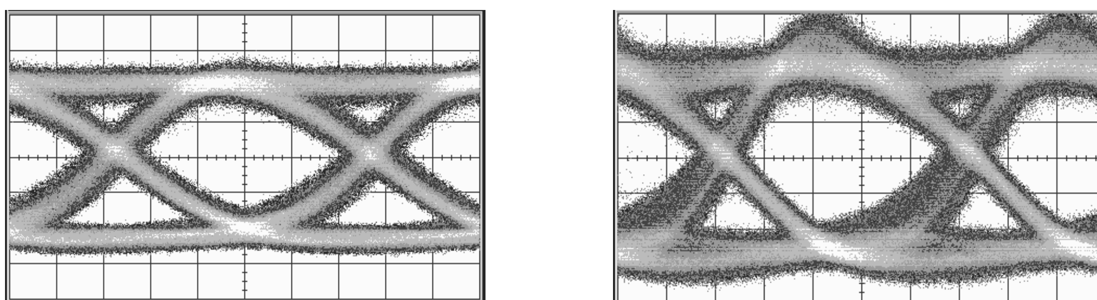

Fig. 8(a) 25°C (b) 85°C eye diagram of SC-VCSEL up to 12.5 Gb/s with 6dB extinction ratio. The scale in the figure is 15 ps/div.

To guarantee the device reliability is always a tough work but a natural task for the components supplier in the data communication markets. We have accumulated life test data up to 1000 hours at 70°C/8mA with exceptional reliability. As shown in Fig. 9, the light output is plotted versus time scale for SC-MQW VCSEL chips under the high temperature operation lifetime (HTOL) test at 70°C/8mA. None of them shows the abnormal behavior.

3. PLANARIZED OXIDE-IMPLANTED VCSEL

The epi-wafers of the planarized oxide-implanted VCSELs were grown by Aixtron 2400 G3 metal-organic chemical vapor-phase deposition (MOCVD) on n^+-GaAs substrate, the structure of which consists of a three quantum-well GaAs/AlGaAs active layer, sandwiched by fully doped n- and p-DBR mirrors. Both n- and p-DBR are composed

Downloaded From: http://proceedings.spiedigitallibrary.org/ on 04/26/2014 Terms of Use: http://spiedl.org/terms

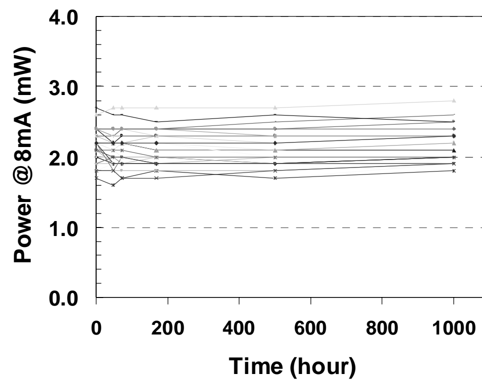

Fig. 9 HTOL (70°C/8mA) performance of the strain compensated VCSEL

of interlaced 1/4λ-thick $Al_{0.15}Ga_{0.85}As$ and $Al_{0.9}Ga_{0.1}As$ layers, with the periods of 39.5 and 22, respectively. The oxide-confined VCSEL process procedure has been described elsewhere [19] [20]. Moreover, the mesa diameter of the fabricated device was 22 μm with a 5 μm oxide aperture, and the device surface was quasi-planar so that the annular p-contact metal and the bond pad were on the same level. The p-contact was created by directly depositing Ti/Pt/Au on the upper heavily doped p^+ GaAs contact layer, and Au/Ge/Ni/Au was deposited on the bottom side of the substrate following thinning down. Notably, the process did not use either the intra-cavity / co-planar metal contact nor the polyimide resin planarization technique. Multiple proton implantations with a dose of 10^{15} cm^{-2} and four different proton energy ranges between 300 to 420keV were adapted according to simulation results of the stopping and range of ions in matter (SRIM). The implantation region was kept away from the mesa to prevent damage to the active region and consequent voiding of triggering reliability issues.

Fig. 10 displays the L-I-V characteristics of the fabricated VCSELs with (solid lines) and without (dashed lines) proton implantation, respectively. The inset in the lower right corner of Fig. 10 is a top view microphotograph of the emitting area. Notably, the L-I-V curves before and after implantation are very similar. This result differs significantly from previous investigation [21], because the mesas were entirely protected during implantation in this study and thus no damage was introduced into the active region. Consequently the threshold current can be maintained at the same value, and the DC characteristics are not influenced. The threshold currents of both samples are 0.5mA and the resistance typically is 90 ohm.

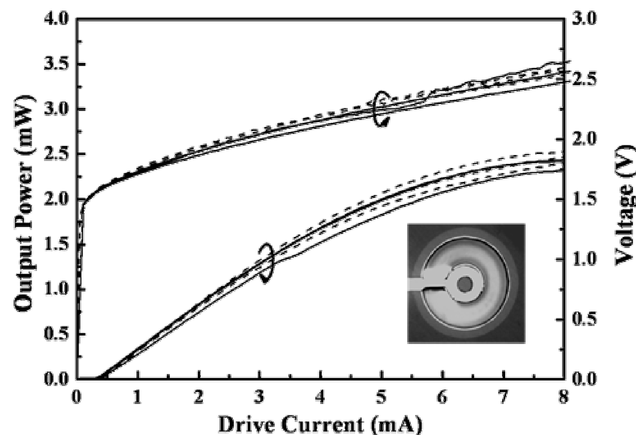

Fig. 10 L-I-V curves of three oxide-implanted VCSELs (solid lines) and three oxide-only VCSELs (dashed lines)

Downloaded From: http://proceedings.spiedigitallibrary.org/ on 04/26/2014 Terms of Use: http://spiedl.org/terms

The small signal modulation responses for both oxide-only VCSEL and oxide-implanted VCSEL are shown in Figs. 11(a) and 11(b) respectively. Fig. 11(a) reveals that the resonance frequency increased with the biasing current as expected. The 3dB frequency was restricted at ~2.3 GHz owing to parasitic cut-off. After proton implantation, a parasitic-free modulation response was obtained as shown in Fig. 11(b). Fig. 12 plots the resonant frequency and 3 dB

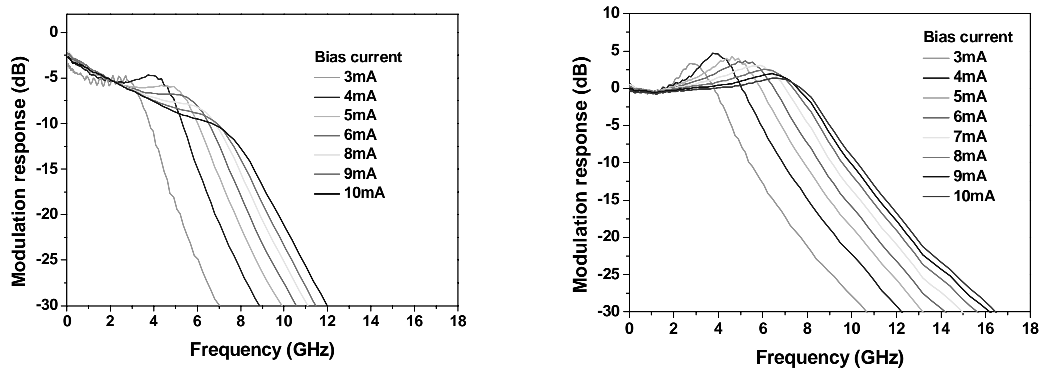

Fig. 11 Small signal modulation response of (a) oxide-only VCSEL (b) oxide-implanted VCSEL

frequency as a function of bias current for both oxide-only and oxide-implanted VCSEL. Fig. 12 clearly indicates that the resonant frequencies are similar for both oxide-only and oxide-implanted VCSELs. However, although the resonant frequency increases with bias current, the 3dB frequency is restricted at ~2.3 GHz for oxide-only VCSEL, while the 3dB frequency of oxide-implanted VCSEL increases with bias current throughout the measurement range. These results clearly show that the parasitic components restricted the modulation bandwidth of oxide-only VCSEL, and moreover that the proton implantation successfully removed the parasitic effect. Fig. 13 shows the eye diagram modulated at 10Gbps with 6mA bias and 6dB extinction ratio for both oxide-only and oxide-implanted VCSELs. For oxide-only VCSEL, the turn on jitter was about 30 ps, and the fall time tail clearly hit the mask. In contrast, the eye improved significantly after ion implantation, and could pass the 10 Gb/s mask. The rise time, fall time and jitter of the oxide-implanted device were 44 ps, 54 ps and 20 ps, respectively.

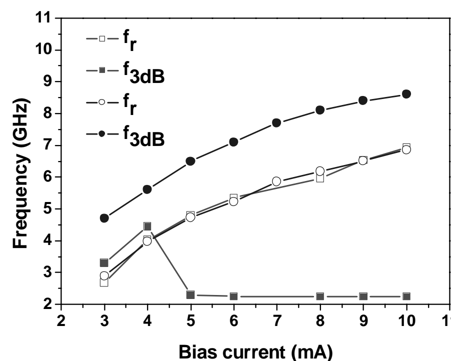

Fig. 12 Resonant frequency and 3 dB frequency for oxide-only VCSELs (square symbol) and oxide-implanted VCSELs (circle symbol)

To further explore how the ion-implantation influenced the electrical parasitic, Fig. 14 illustrates the reflection coefficient (S_{11}) of the oxide-only VCSEL and oxide-implanted VCSEL. The reflection coefficient curves reveal that more RF power is reflected back from the oxide-only VCSEL and therefore degrades the modulation bandwidth. The electrical bandwidth for oxide-only devices is ~ 3 GHz, and exceeds 20 GHz for oxide-implanted devices. This finding again confirms that the proton-implantation has successfully reduced the parasitic capacitance. An equivalent circuit model shown in Fig. 15 was used to extract the circuit components. The resistance Rm represents the mirror loss, while the Ra accounts for the active region resistance. Ca represents a combination of the capacitance of the active area and

Downloaded From: http://proceedings.spiedigitallibrary.org/ on 04/26/2014 Terms of Use: http://spiedl.org/terms

oxide layer. A shunt resistance Rp is also included to account for pad loss, and the pad capacitance is represented by Cp. This equivalent circuit can also be applied to examine the extrinsic limitations on the modulation speed and to determine the influence of parasitic capacitance and mirror resistance on the modulation bandwidth. The values of the circuit components were extracted using ADS (Advanced Design System, Agilent) by fitting both the magnitude and phase of S_{11} over the measured frequency range. Based on a co-optimization at several bias conditions, Rm was around 42 ohm and Ra was found to be bias dependent, varying from 80 to 37 ohm in 1~6 mA. The major difference between oxide-only and oxide-implanted devices was the capacitance Ca and Cp. Moreover, the Ca and Cp of oxide-only devices were 1.8 and 0.4 pF, respectively, while the Ca and Cp of oxide-implanted devices were 0.5 and 0.28 pF, respectively. Therefore, proton-implantation is shown to effectively reduce the bond pad capacitance and oxide capacitance.

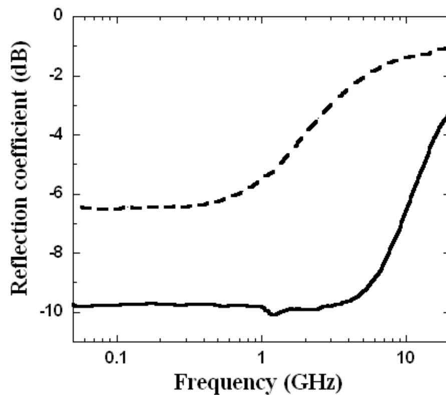

Fig. 14 Reflection coefficient (S_{11}) for oxide-only device (dashed line) and oxide-implanted device (solid line) at 3 mA

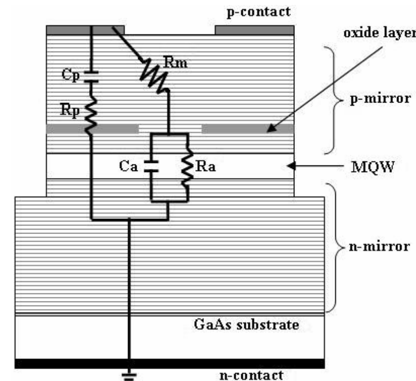

Fig. 15 Equivalent circuit used for the oxide confined VCSEL impedance.

CONCLUSION

In conclusion, we demonstrated that SC-MQW VCSELs show very low threshold current good temperature performance, and high modulation response up to 12.5 Gb/s from 25°C to 85°C. In addition, low cost, high speed (10 Gb/s) oxide-implanted VCSEL were presented. Both approaches are making the 10Gb/s VCSEL promising in the optoelectronic and other commercial applications in the coming days.

REFERENCE

1. J. A. Tatum, A. Clark, J. K. Guenter, R. A. Hawthorne, and R. H. Johnson, "Commercialization of Honeywell's VCSEL technology," *Vertical-Cavity Surface-Emitting Lasers IV*, K. D. Choquette and C. Lei, editors, Proceedings of the SPIE, vol. 3946, pp. 2-13, SPIE, Bellingham, WA, 2000..
2. F. H. Peters and M. H. MacDougal, "High-Speed High-Temperature Operation of Vertical-Cavity Surface-Emitting Lasers" IEEE Photon. Technol. Lett., vol. 13, No 7, p. 645–647, July 2001.
3. F. H. Peters, D. J. Welch, V. Jayaraman, M. H. MacDougal, J. D. Tagle, T. A. Goodwin, J. E. Schramm, T. D. Lowes, S. P. Kilcoyne, K. R. Nary, J. S. Bergey, and W. Carpenter, "10 Gb/s VCSEL-based data links," Photonics West, San Jose, CA, Tech. Rep. OE 3946–26, 2000.
4. C.W. Wilmsen, H. Temkin, and L.A. Coldren, eds., *Vertical-Cavity Surface-Emitting Lasers: Design, Fabrication, Characterization, and Applications*, Cambridge University Press, 1999.
5. K. L. Lear, M. Ochiai, V. M. Hietala, H. Q. Hou, B. E. Hammons, J. J. Banas, and J. A. Nevers, "High-speed vertical cavity surface emitting lasers," in *Dig. IEEE/LEOS Summer Topical Meetings*, 1997, pp. 53–54.
6. J. A. Lehman, R. A. Morgan, M. K. Hibbs-Brenner, and D. Carlson, "High-frequency modulation characteristics of hybrid dielectric/AlGaAs mirror singlemode VCSELs," *Electron. Lett.*, vol. 31, pp. 1251-1252, 1995.

Downloaded From: http://proceedings.spiedigitallibrary.org/ on 04/26/2014 Terms of Use: http://spiedl.org/terms

7. K. L. Lear, A. Mar, K. D. Choquette, S. P. Kilcoyne, R. P. Schneider, Jr., and K. M. Geib, “High-frequency modulation of oxide confined vertical cavity surface emitting lasers,” *Electron. Lett.*, vol. 32, pp. 457–458, 1996.
8. L. J. Mawst, S. Rusli, A. Al-Muhanna, and J. K. Wade, “Short-wavelength (0.7 μm < λ <0.78 μm) high-power InGaAsP-active diode lasers,” *IEEE J. Select. Topics Quantum Electron.*, vol. 5, pp. 785–791, (1999).
9. N. Tansu, D. Zhou, and L. J. Mawst, “Low Temperature Sensitive, Compressively-Strained InGaAsP Active (λ=0.78-0.85 μm) Region Diode Lasers,” *IEEE Photon. Technol. Lett.*, Vol.12(6), pp.603-605 , 2000.
10. T. E. Sale, C. Amamo,Y. Ohiso, and T.Kurokawa, “Using strained lasers (AlGa) In As P system materials to improve the performance of 850 nm surface- and edge-emitting lasers,” *Appl. Phys. Lett.*, vol. 71, p. 1002–1004, (1997).
11. N. Tansu, L.J Mawst, “Compressively-strained InGaAsP-active (λ=0.85μm) VCSELs” *IEEE Lasers and Electro-Optics Society 2000 Annual Meeting. LEOS 2000.* vol. 2, p. 724 -725 (2000).
12. H. C. Kuo, Y. S. Chang, F. I. Lai, T. H. Hsueh, “High speed modulation of 850 nm InGaAsP/InGaP strain-compensated VCSELs. Electon. Lett. Vol 39, p. 1051-10523 (2003)
13. David J. Bossert, Doug Collins, Ian Aeby, J. Bridget Clevenger, “Production of high-speed oxide confined VCSEL arrays for datacom application” Photonics West, San Jose, CA, p.p 142 Proc. SPIE Vol. 4649 (2002)
14. http://www.ieee802.org/
15. Thibeault BJ, Bertilsson K, Hegblom ER, “High-speed characteristics of low-optical loss oxide-aperture vertical-cavity laser,” IEEE Photon. Technol. Lett., vol. 9, pp. 11-13, Jan. 1997
16. L. A. Coldren and S. W. Corzine, *Diode Lasers and Photonic Integrated Ciurcuits.* New York: Wiley, 1995, pp. 201-204
17. T. R. Chen, B. Zhao, L. Eng, Y. H. Zhuang, “Very high modulation efficiency of ultralow threshold current single quantum well InGaAs lasers”, Electon. Lett., Vol. 29, p. 1525-1526 (1993)
18. Sven Eitel, Stephan Hunziker, Dominique Vez, “Multimode VCSELs for high bit-rate and transparent low-cost fiber-optic links”, p183 Proc. SPIE Vol. 4649 (2002)
19. H.C. Yu, S.J. Chang, Y.K. Su, C.P. Sung, Y.W. Lin, H.P. Yang, C.Y. Huang, J.M. Wang**,** *CLEO PR* 2003, Conference Digest, pp. 159, 2004
20. H.C. Yu, S.J. Chang, Y.K. Su, C.P. Sung, Y.W. Lin, H.P. Yang, C.Y. Huang, J.M. Wang, *Mater. Sci. Engi. : B.*, to be published.
21. K.D. Choquette , A.J. Fischer, K.M. Geib , G.R.Hadley, A.A. Allerman, J.J. Hindi, *Semiconductor Laser Conference*, Conference Digest, pp.59 –60, 2000.

* E-mail: hckuo@faculty.nctu.edu.tw; phone: 886-3-5712121 ext 31986; fax: 886-3-5716631

Downloaded From: http://proceedings.spiedigitallibrary.org/ on 04/26/2014 Terms of Use: http://spiedl.org/terms